Assessment of an Integrated Approach for Predicting As-Quenched Microstructure and Jominy Hardenability Curve of Low-Alloy Steels






A computational framework was developed to solve a two-dimensional transient heat transfer equation using the finite difference method, enabling simulation of the cooling behavior of Jominy specimens. By integrating cooling rates from different positions along the Jominy specimen with calculated continuous cooling transformation diagrams, the volume fractions of the steel constituents as a function of distance from the quenched end were predicted. This approach allowed the construction of Jominy hardenability curves for two selected low-alloy steels. The simulated results exhibited reasonable agreement with experimental measurements for a boron-free steel. However, for boron-containing steels, the methodology needs additional modeling considerations to capture boron's effect on hardenability.

Authors

Diego de Araujo Santana (top left), R&D Engineer, Vallourec South America, Jeceaba, MG, Brazil
diego.santana@vallourec.com

Gabriel Filipe Oliveira, R&D Intern, Vallourec South America, Jeceaba, MG, Brazil
gabriel.foliveira@ext.vallourec.com

Gabriel Jorge (top right), R&D Engineer, Vallourec South America, Jeceaba, MG, Brazil
gabriel.jorge@vallourec.com

Michel Piette (bottom left), Metallurgy Principal Engineer, Vallourec Tubes France, Aulnoye-Aymeries, France
michel.piette@vallourec.com

Vicente Braz Trindade (bottom right), R&D General Manager, Vallourec South America, Jeceaba, MG, Brazil
vicente.trindade@vallourec.com

Introduction

Understanding and predicting the hardenability of low-alloy steel is essential for tailoring its composition and meeting the demands of industry. Among the various characterization techniques, the Jominy end-quench test remains a widely adopted method for evaluation of steel hardenability. However, experimental determination of Jominy curves is time-consuming, especially when evaluating multiple alloy compositions. To address this challenge, computational approaches have emerged as powerful alternatives, offering predictive capabilities that can accelerate materials design and optimization.

In the literature, methodologies that integrate cooling paths with continuous cooling transformation (CCT) diagrams are widely employed to predict microstructural evolution[1,2] and residual stress in welds[3,4] of low-alloy steels. These integrated approaches are commonly regarded as powerful tools for alloy design, for assessing the influence of individual alloying elements and for evaluating the impact of processing parameters on the final microstructure.

In this work, the proposed method was applied for predicting Jominy curves. A two-dimensional transient heat transfer simulation of the Jominy test was carried out using the Finite Difference Method (FDM),[5] enabling the calculation of cooling rate at various distances along the specimen. An open-source algorithm for generating CCT diagrams[6] was then employed to predict the evolution of microstructural constituents as a function of Jominy distance. This algorithm requires only the chemical composition and austenite grain size as input, allowing quick prediction of phase transformations during cooling. Finally, by coupling the calculated cooling rate with the predicted CCT data, the hardness profiles were calculated using empirical relationships.

To evaluate the proposed method, two low-alloy steels with similar hardenability were selected: one boron-free and one boron-containing. The results showed reasonable agreement between simulations and experiments for the boron-free steel. However, for the boron-containing steel, the method yielded poor agreement. Each stage of the calculation was critically examined, and insights are provided on the methodological limitations and potential improvements needed to enhance the model's accuracy.

Materials and Methods

Materials: Two low-alloy steels with comparable critical cooling rates for martensite formation, but differing chemical compositions, were selected to evaluate the accuracy of the integrated modeling approach. In this study, these steels are designated as Steel A and Steel B, and their chemical compositions (in weight percentage) are presented in Table 1.

Table 1

Chemical Composition of Two Selected Steels Used for Predicting the As-Quenched Microstructure and Jominy Hardenability of Low-Alloy Steels Through the Integrated Modeling Approach

	C	Mn	Cr	Mo	V	Nb	Ti	B
Steel A	0.34	0.30–0.50	0.90–1.10	1.25	Yes	Yes	No	No
Steel B	0.29			0.80	No	Yes	Yes	Yes

Methods

Cooling Modeling — Under transient conditions with constant thermophysical properties, the heat diffusion equation in two dimensions (2D), x and z, is given by Eq. 1:[5]

$$\frac{\partial T}{\partial t}=\alpha\left(\frac{\partial^2 T}{\partial x^2}+\frac{\partial^2 T}{\partial z^2}\right)+\frac{\dot{q}}{\rho c_p} \quad \text{(Eq. 1)}$$

where

T = the temperature,

t = the time,

$\dot{q}$ = the rate of energy generation per unit volume and

α = the thermal diffusivity of the material, given by ($\alpha = k/(\rho.c_p)$), in which k is the thermal conductivity, ρ is the density, and c_p is the specific heat at constant pressure.

The thermophysical properties (k, ρ and c_p) vary with temperature and steel composition.[5] However, as argued by Li et al.,[7] such variations have a negligible effect on the cooling rates during Jominy test. Therefore, in this work, they were assumed constant and average values of ρ = 7,800 kg/m^3, k = 45 W/m.K, and c_p = 500 J/kg.K were used.

The rate of energy generation, such as the latent heat associated with austenite decomposition,[8] may change the cooling rate along the axial positions in the Jominy specimen. For sake of simplicity, it was not considered in this study, but future work will investigate the effects of including latent heat on the cooling rate and microstructure predictions.

For calculating the cooling throughout the Jominy specimen, Eq. 1 was discretized by using the explicit FDM method.[5] The time derivative at the (m, n) nodal point was approximated by Eq. 2, whereas the second-order temperature gradient along radial (x) and axial (z) directions were approximated by Eqs. 3 and 4, respectively. The p sob script indicates the step number in time. The Δt, Δx and Δz are the discrete intervals for t, x and z.

$$\left.\frac{\partial T}{\partial t}\right|_{m,n}\approx\frac{T_{m,n}^{p+1}-T_{m,n}^{p}}{\Delta t} \quad \text{(Eq. 2)}$$

$$\left.\frac{\partial^2 T}{\partial x^2}\right|_{m,n}\approx\frac{T_{m-1,n}^{p}-2T_{m,n}^{p}+T_{m+1,n}^{p}}{(\Delta x)^2} \quad \text{(Eq. 3)}$$

$$\left.\frac{\partial^2 T}{\partial z^2}\right|_{m,n}\approx\frac{T_{m,n-1}^{p}-2T_{m,n}^{p}+T_{m,n+1}^{p}}{(\Delta z)^2} \quad \text{(Eq. 4)}$$

After substituting Eqs. 2, 3 and 4 in Eq. 1, and considering a square grid ($\Delta x = \Delta z$), the temperature at internal nodes can be calculated using Eq. 5.

$$T_{m,n}^{p+1}=Fo\left(T_{m+1,n}^{p}+T_{m-1,n}^{p}+T_{m,n+1}^{p}+T_{m,n-1}^{p}\right)+(1-4Fo)T_{m,n}^{p} \quad \text{(Eq. 5)}$$

where Fo = the Fourier number, given by $Fo = (\alpha.\Delta t)/(\Delta x)^2$.

For the nodal points at the surface and corners of the Jominy specimen, a convective boundary condition was assumed. From energy conservation balance, the general Eqs. 6 and 7 are used for nodes at surfaces and the corner, respectively.

$$T_{m,n}^{p+1}=Fo\left(2T_{m-1,n}^{p}+T_{m,n+1}^{p}+T_{m,n-1}^{p}+2BiT_{\infty}\right)+(1-4Fo-2BiFo)T_{m,n}^{p} \quad \text{(Eq. 6)}$$

$$T_{m,n}^{p+1} = 2Fo\left(T_{m-1,n}^{p} + T_{m,n-1}^{p} + 2BiT_{\infty}\right) + \left(1 - 4Fo - 4BiFo\right)T_{m,n}^{p}$$

(Eq. 7)

where Bi is the Biot number, given by $Bi = (h.\Delta x)/k$, in which h is the convective heat transfer coefficient. This variable, for water and still air, change as a function of temperature.[9,10] In this work, they were assumed constant and having average values of 10,000 W/m^2.K and 40 W/m^2.K, respectively.

A schematic illustration of the Jominy specimen displaying the grid geometry (number of nodes and grid spacing) as well as the boundary conditions used in the formulation of the problem is shown in Fig. 1.

In addition to the 2D-FDM, a one-dimensional analytical solution of the heat-transfer equation for a semi-infinite solid with a convective boundary condition[11] was employed to calculate the temperature evolution in the Jominy specimen. The analytical formula is provided in Eq. 8.

$$\frac{T(z,t) - T_i}{T_{\infty} - T_i} = erfc\left(\frac{z}{2\sqrt{\alpha t}}\right) - \left[\exp\left(\frac{hz}{k} + \frac{h^2\alpha t}{k^2}\right)\right]\left[erfc\left(\frac{z}{2\sqrt{\alpha t}} + \frac{h\sqrt{\alpha t}}{k}\right)\right]$$

(Eq. 8)

where

$T(z,t)$ = the temperature at distance z at time t,

T_i = the initial temperature of the solid,

T_{∞} = the environment temperature,

α = the thermal diffusivity of the material,

k = the thermal conductivity,

h = the convective heat transfer coefficient and

$erfc$ = the complementary error function.

Continuous Cooling Transformation Diagram — The CCT diagrams were calculated using an open-source algorithm[6] based on the semiempirical model originally proposed by Kirkaldy et al.,[12] and subsequently modified by Li et al.[7] In this model, the time required for

Figure 1

Grid geometry and boundary conditions used for solving the heat transfer equation using the explicit finite difference method.

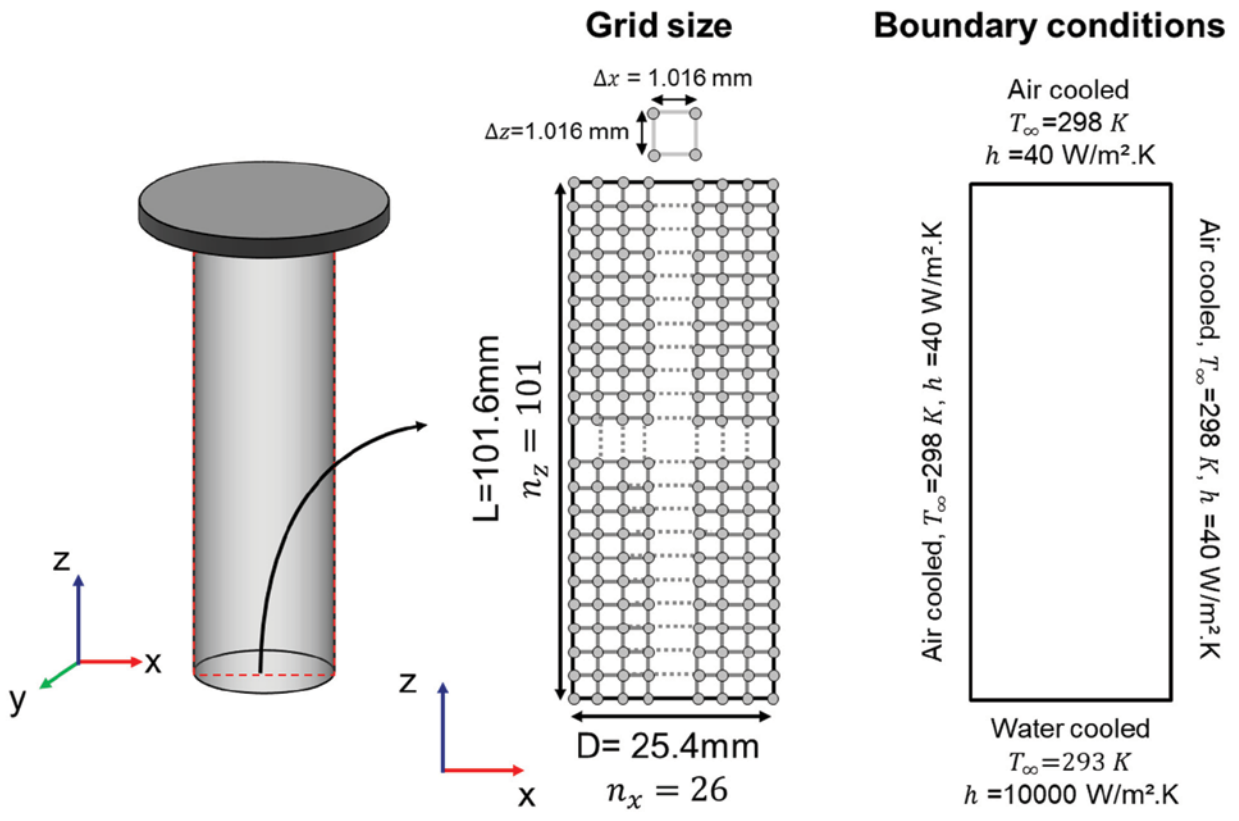

the isothermal decomposition of a fraction X of austenite into ferrite, pearlite or bainite at a given temperature T is described by the general form of Eq. 9.

$$\tau(X,T) = \frac{1}{2^{\beta G}} e^{\left(\frac{Q_{eff}}{RT}\right)} F(comp.) \frac{1}{\Delta T^{q}} \int_{0}^{X} \frac{dX}{X^{0.4(1-X)}(1-X)^{0.4X}}$$

(Eq. 9)

where the term $\frac{1}{2^{\beta G}}$ accounts for the influence of previous austenite grain size on transformation kinetics, being G the ASTM prior austenite grain size and β an empirical constant. The term $e^{\left(\frac{Q_{eff}}{RT}\right)} F(comp.)$ relates to the effective diffusion coefficient involving the alloying elements in the steel, with Q_{eff} denoting the effective activation energy for diffusion, R is the gas constant, and $F(comp.)$ an empirical function based on the nominal concentration (in wt. %) of the alloying elements in the steel. The function F for ferrite, pearlite and bainite are given in Eqs. 10–12. The undercooling, ΔT, is defined as the temperature difference relative to the maximum temperature at which a given transformation starts. For ferrite formation, the undercooling is expressed as $\Delta T = Ae_3 - T$, for pearlite $\Delta T = Ae_1 - T$ and for bainite $\Delta T = Bs - T$. The Ae_3, Ae_1 and Bs temperatures are estimated using empirical formulas derived from experimental data. The exponent n is related to the dominant diffusion mechanism: n = 3 corresponds to boundary diffusion, typical of ferrite and pearlite transformations, while n = 2 corresponds to volume diffusion, characteristic of bainite formation.

$$F_{Ferrite} = \exp\left(\begin{matrix}1.00 + 6.31C + 1.78M + 1.12Ni \\ +2.70Cr + 4.06Mo + 0.31Si\end{matrix}\right)$$

(Eq. 10)

$$F_{Pearlite} = \exp\left(\begin{matrix}-4.25 + 4.12C + 4.36Mn + 1.71Ni + \\ 3.33Cr + 5.19\sqrt{Mo} + 0.44Si\end{matrix}\right)$$

(Eq. 11)

$$F_{Bainite} = \exp\left(\begin{matrix}-10.23 + 10.18C + 0.85Mn + \\ 0.55Ni + 0.90Cr + 0.36Mo\end{matrix}\right)$$

(Eq. 12)

In summary, the model proposes an individual isothermal kinetic equation for austenite decomposition into ferrite, pearlite and bainite. The full equation for each transformation is detailed in Reference 6. Graphically, for a fixed temperature, Eq. 9 displays a sigmoidal behavior when the transformed fraction is plotted as a function of time.

For predicting the transformation of austenite to martensite, a modified Koistinen–Marburger (K-M)[13] equation is used:[6]

$$\frac{X_M}{X_A^0} = 1 - \exp\left[\frac{\ln(0.01)}{M_s - M_f}(M_s - T)\right]$$

(Eq. 13)

where

X_M = the martensite volume fraction at temperature T,

X_A^0 = the austenite volume fraction at the start of the martensite transformation,

M_s = the martensite start temperature and

M_f = the martensite finish temperature.

Finally, to convert between isothermal to nonisothermal behavior, the Scheil additivity rule[14] is adopted,

$$\int_{0}^{t_{CCT}} \frac{dt}{\tau(T)} = 1 \cong \sum_{0}^{t_{CCT}} \frac{\Delta t}{\tau(T)} = 1$$

(Eq. 14)

where

Δt = the time step,

$\tau(T)$ = the incubation time for transformation at temperature T and

t_{CCT} = the time at which the nonisothermal transformation begins.

Hardness Prediction — The Vickers hardness distribution along the Jominy specimen was calculated using Eqs. 15–18 developed by Maynier et al.,[15] which incorporate the volume fraction of microstructural constituents (X), the nominal concentrations of alloying elements (in wt. %), and the cooling rate at 700°C, denoted as V' (in °C/hour). The subscripts *fp*, *f*, *p*, *b* and *m* refer to ferrite–pearlite, ferrite, pearlite, bainite, and martensite, respectively. The overall hardness is determined using Eq. 15, while the hardness contributions from ferrite–pearlite, bainite, and martensite are calculated using Eqs. 16, 17 and 18, respectively.

$$H = H_{fp}(X_f + X_p) + H_b X_b + H_m X_m$$

(Eq. 15)

$$H_{fp} = 42 + 223C + 53Si + 30Mn + 12.6Ni + 7Cr + 19Mo + (10 - 19Si + 4Ni + 8Cr + 130V)\log V'$$

(Eq. 16)

$$H_b = -323 + 185C + 330Si + 153Mn + 65Ni + 144Cr + 191Mo + (89 + 53C - 55Si - 22Mn - 10Ni - 20Cr - 33Mo)\log V'$$

(Eq. 17)

$$H_m = 127 + 949C + 27Si + 11Mn + 8Ni + 16Cr + 21\log V'$$

(Eq. 18)

The formulae are argued to be valid within the following concentration range (in wt. %): 0.2 < C < 0.5%, Si < 1%, Mn < 2%, Ni < 4%, Cr < 3%, Mo < 1% and V < 0.2%.[15]

Results and Discussion

Fig. 2 shows the temperature distribution throughout the Jominy specimen at different cooling times. Following the Jominy test, hardness is measured at multiple locations along the z-axis, at depths exceeding 0.38 mm from the outer surface.[16] If the cooling rate near the surface differs from that at the center of the specimen, the resulting microstructure and, thus, the hardness, may also differ. The calculations show that the temperature field exhibits a flat cooling front, with negligible temperature gradient across the Jominy specimen radius. This is justified by the fact that the heat transfer by conduction through the quenched end is significantly more effective than heat loss by convection along the lateral surface. Therefore, the difference in the temperature profile and, consequently, in the cooling rate at the center and near the lateral surface is negligible.

Fig. 3a shows the temperature as a function of time at different axial distances from the quench end during

Figure 2

Temperature distribution throughout Jominy specimen at 1, 10, 60, 300 and 600 seconds.

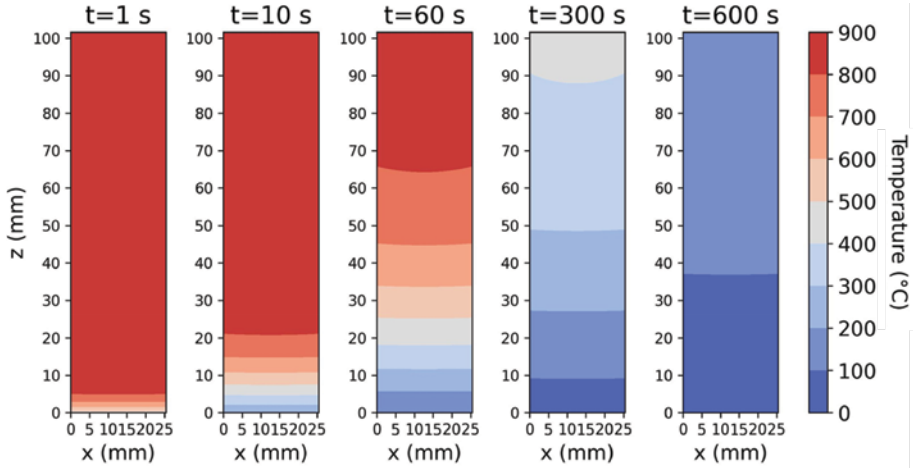

Figure 3

Temperature as a function of time for different distance from the quench end in the Jominy specimen (a) and cooling rate at 700°C as a function of distance from the quench end (b).

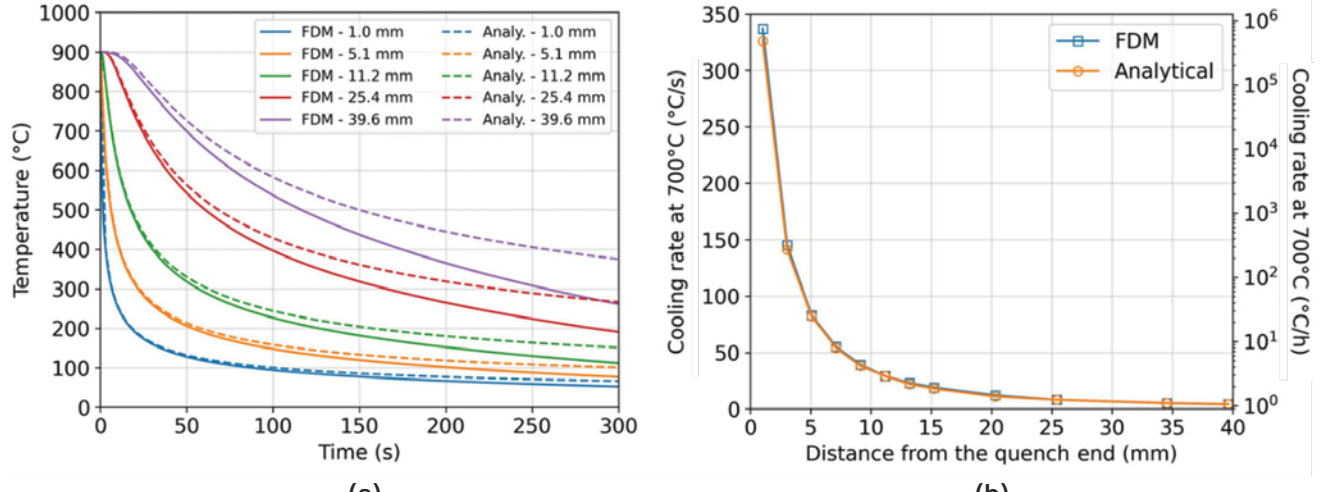

(a) (b)

the first 5 minutes of the Jominy test. This figure presents both the thermal profile calculated using the 2D-FDM and the analytical formula. The results are in good agreement with experimental data of instrumented Jominy test and calculation carried out using different approaches, such as finite element method.[7]

The 2D-FDM and the analytical solution exhibit close agreement for cooling times up to ~50 seconds. As cooling progresses, however, the temperature prediction between the two approaches begins to diverge, particularly at locations farther from the quenched end. This behavior can be attributed to the assumptions inherent in the one-dimensional analytical solution, where heat loss is considered only from the quench end. In contrast, the 2D-FDM accounts for heat transfer contributions from the upper surface, lateral surfaces and the quench end. Consequently, the 2D-FDM model predicts higher overall heat extraction, especially at positions more distant from quenched surface.

The cooling rate at 700°C along different axial distances in the Jominy specimen is displayed in Fig. 3b. This parameter was calculated from both the 2D-FDM and analytical results. The cooling rate at 700°C is usually used as reference since Maynier et al.[15] observed a linear relationship between the logarithm of the steel bar diameter (or plate thickness) and the logarithm of the cooling rate at 700°C (expressed in °C/hour) using different cooling media.

Although some deviation exists between the temperature profiles as a function of time calculated using the 2D-FDM and the analytical solution, the cooling rates at 700°C are very similar in both approaches, regardless of the distance from the quench end. This similarity arises because the temperature drop to 700°C is nearly identical in both cases, indicating that the influence of lateral surface heat losses, accounted for in the 2D-FDM but neglected in the 1D analytical solution, remains relatively minor within this temperature range. Consequently, cooling in this interval is dominated by heat extraction through the quenched end, which explains the close agreement between the cooling rates predicted by the two methods at 700°C.

The predicted CCT diagrams for Steels A and B are displayed in Fig. 4a and 4b, respectively. The characteristic temperatures Ae_1 and M_s for both steels are well described by the model, but Ae_3 is underestimated when compared to experimental data. The diagrams show a different behavior between both steels. Steel A shows a critical cooling for martensite formation of ~25°C/second, whereas in steel B it is ~100°C/second. The experimental cooling rates for martensite formation in these steels are 15°C/second and 10°C/second, respectively. Furthermore, the calculated ferrite and pearlite start curves are also shifted for longer cooling times in Steel A. Experimental CCT data (not presented here) shows a good agreement with predicted behavior of Steel A.

Boron is a well-known element that can enhance the hardenability of steel when properly adjusted. Small additions of boron (on the order of 10–30 wt. ppm) tend to increase the steel hardenability by retarding the nucleation of allotriomorphic ferrite and, to a lesser extent, the nucleation of bainite.[17,18] However, beyond a certain concentration, the effect may become the opposite. At low levels, boron atoms segregate to austenite grain boundaries, lowering their interfacial energy.[19] This makes such boundaries less effective as heterogeneous nucleation sites. With increasing boron content, boride particles may form at prior austenite grain boundaries, favoring the ferrite nucleation, which reduces hardenability.[17,18] Consequently, in a well-designed boron-containing low-alloy steel, the transformation curves for ferrite, and to some extent for bainite, are shifted toward longer cooling times.

Figure 4

Calculated CCT diagrams for Steel A (a) and Steel B (b).

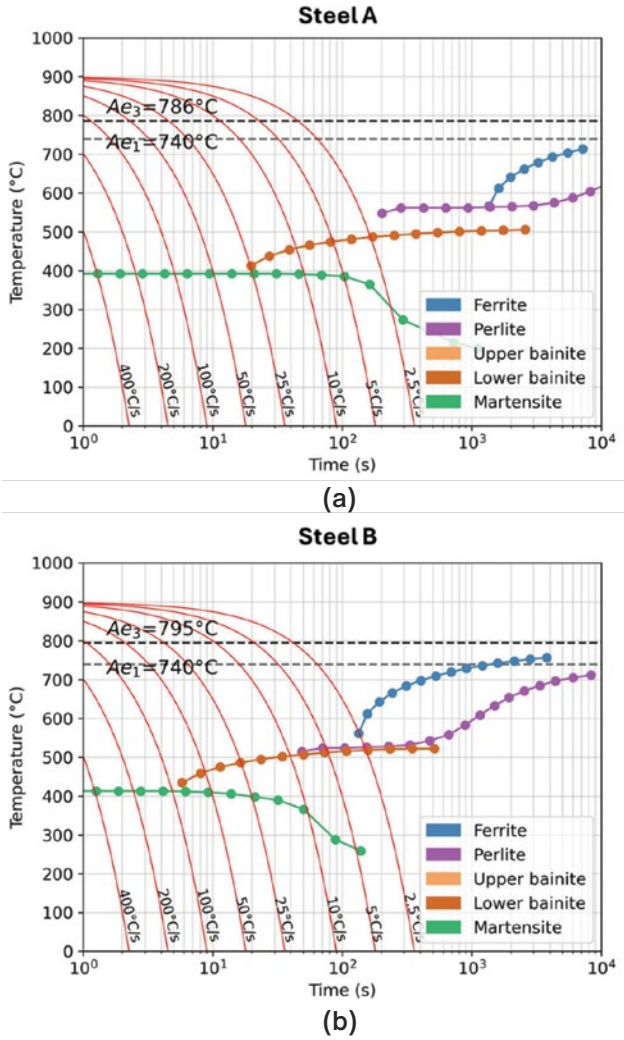

As shown in Eqs. 10–12, the CCT model does not incorporate the effect of boron and, therefore, it is not suitable for the design of boron-containing steels. Conversely, the model reproduced the CCT diagram of boron-free steel with reasonable accuracy when compared to experimental data, demonstrating its usefulness as a tool for designing low-alloy steels without boron.

It is worth noting that, unlike most alloying elements, which generally increase the hardenability of steel as their concentration rises, the effect of boron is dual in nature. Consequently, incorporating the influence of boron into the modeling process is particularly challenging. This requires the development of kinetic equations capable of accounting not only for this dual behavior of boron but also for its interactions with the other alloying elements. For example, boron has a high affinity with nitrogen, and the formation of nitrogen borides leads to a lower availability of free boron to segregate grain boundaries, reducing the hardenability for a given boron content depending on nitrogen availability.[17,18]

Fig. 5 shows the predicted fractions of microstructural constituents for Steels A and B along the Jominy distance. The correlation between the CCT diagrams and the Jominy positions was established by assuming an equivalence between the cooling rate at 700°C in the Jominy specimen and the constant cooling rate employed in constructing the CCT diagrams.[15,20] For instance, at a distance of 5 mm from the quench end, the calculated cooling rate at 700°C is equal to 83°C/second. Using this cooling rate, the fraction of the constituents was then calculated through the CCT algorithm.

For Steel A, the microstructure is expected to remain fully martensitic up to approximately 13 mm from the quenched end. Beyond this point, it transitions to a mixture of martensite and bainite, with the martensite fraction gradually decreasing as the distance increases. In contrast, for Steel B, the microstructure is expected to be fully martensitic only up to about 5 mm from the quenched end. At greater distances, the martensite fraction decreases rapidly, indicating a faster loss of hardenability relative to Steel A. As will be shown latter, the experimental hardness results show an opposite behavior: for Steel A, the hardness decreases more rapidly as a function of Jominy distance than for Steel B.

The use of equivalent cooling criteria to relate the results of Jominy tests and CCT diagrams remains an open topic in the literature. In addition to the equivalence criterion of cooling rate at 700°C, another criterion often employed is the equivalence of the time required to cool from Ac_3 to 500°C[21] or from 800 to 500°C[22] in Jominy specimen with that of CCT diagrams. A further common practice involves superimposing the Jominy thermal profile onto the CCT diagram to predict the fractions of the constituents. All these assumptions are argued to result in errors, since CCTs are developed using constant cooling rates. In contrast, the cooling rate in the Jominy test is not constant, as can be deduced from Fig. 3a. Therefore, the errors associated with these equivalent criteria must be critically assessed to evaluate their validity.

Figure 5

Fraction of constituents along the distance from quench end for Steel A (a) and Steel B (b).

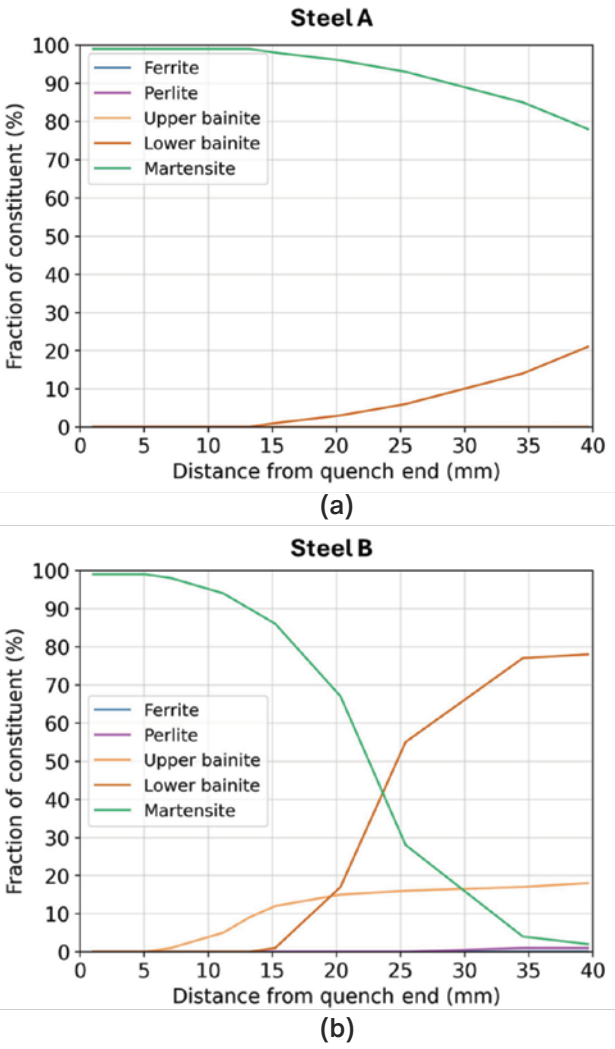

Fig. 6a and 6b show the experimental data and calculated results for Steel A and B, respectively. The conversion from HV scale, calculated using Eq. 13, to Rockwell C scale was performed following the ASTM E140 standard.[23] From the plateau observed in the experimental hardness data, the true martensite depth in the Jominy specimen is approximately 9 mm for Steel A and about 13 mm for Steel B. The results show a reasonable agreement with constituent prediction displayed in Fig. 5 for steel A (fully martensite up to 13 mm). On the other hand, for Steel B, the correspondence between martensite depth prediction (fully martensite up to 5 mm) and experimental results (13 mm) is poor.

The hardness profiles are not well captured by the integrated approach. The discrepancies may arise from

Figure 6

Calculated and experimental data of Jominy hardness profile for Steel A (a) and Steel B (b).

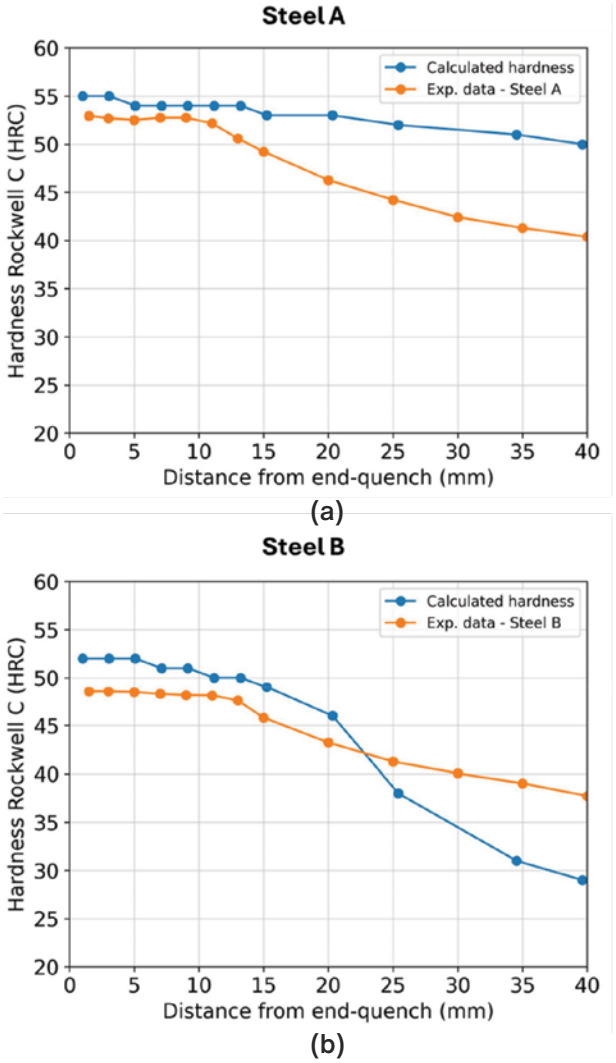

inaccuracies in the predicted constituent fractions, inaccuracies in the hardness equation or a combination of both. Since the calculated hardness varies linearly with the constituent fractions (Eq. 15), any error in the predicted fraction of a given constituent directly scales with the hardness of that constituent. Consequently, inaccuracies in the martensite fraction prediction produce the largest deviations from the true hardness values, followed by bainite and pearlite, for a fixed composition and cooling rate.

Errors may also arise from the hardness equations assigned to each constituent. For example, up to 5 mm from the quenched end, both the model predictions and experimental observations suggest a fully martensitic microstructure. Thus, the calculated hardness should closely match the measured values, but a discrepancy of approximately 2–3 HRC is observed. According to Eq. 18, martensite hardness is influenced by cooling rate. However, different works in the literature suggest that the hardness of fully formed martensite is a function of carbon only.[24,25]

Given these conflicting interpretations, the available data does not permit a definitive attribution of the hardness deviations to either (i) errors in constituent fraction prediction or (ii) inaccuracies in the constituent hardness equations. Further investigation is therefore required to isolate and quantify the contribution of each source of error.

Overall, the integrated approach provides reasonable agreement in predicting both the cooling rate distribution along the Jominy specimen and the CCT diagrams for boron-free steels. However, in the case of boron-containing steels, the isothermal kinetic equation governing austenite decomposition requires revision to improve the accuracy of the predictions. Moreover, additional investigation into the hardness-prediction methodology is necessary, as it is not currently possible to determine whether the discrepancies between calculated and experimental values arise from inaccuracies in constituent-fraction predictions or from limitations in the constituent hardness equations. Therefore, expanding the experimental data set and conducting a broader validation are essential steps toward more robust assessment and enhancement of the model's predictive capability.

Conclusions

In this work, an integrated approach, often used in the literature to predict the hardenability of low-alloy steels, was tested against experimental data of two selected low-alloy steels with close hardenability: one boron-free (Steel A) and another containing boron (Steel B). From the results the following conclusions can be drawn:

- The temperature profile along the different Jominy distances as well as the calculated cooling rate were well captured by solving the 2D transient heat transfer using the finite difference method.
- The calculations show that the temperature field in the Jominy specimen exhibits a flat cooling front, with negligible temperature gradient across the Jominy specimen radius.
- The analytical one-dimensional solution for heat transfer equation with convective boundary condition shows a good agreement with the calculation using the 2D-FDM method.
- The CCT calculations show good agreement for Steel A but poor agreement for Steel B, indicating that the current model is not adequate for steels containing boron.
- The isothermal kinetic equation for austenite decomposition in boron-containing steels should be modified to account for the effect of boron,

which can delay or accelerate the transformation depending on its content.

- The Jominy hardness profiles are not well captured by the integrated approach. Based on the analyzed data, it was not possible to determine whether the observed discrepancies arise primarily from inaccuracies in the predicted phase fractions, from limitations in the hardness equations for the individual constituents, or a combination of both.

This article is available online at AIST.org for 30 days following publication.

References

1. J. Chipalkatti, "Modeling of Austenite Decomposition in an AISI 4140 Steel," thesis, The University of British Columbia, Canada, 1999.
2. A. Malakizadi, "Simulation of Cooling Behavior and Microstructure Development of PM Steels," thesis, Chalmers University of Technology, Sweden, 2010.
3. C.J. Hamelin et al., "Validation of a Numerical Model Used to Predict Phase Distribution and Residual Stress in Ferritic Steel Weldments," *Acta Materialia,* Vol. 75, Aug. 2014, pp. 1–19, doi: 10.1016/j.actamat.2014.04.045.
4. Y.L. Sun et al., "Impact of Weld Restraint on the Development of Distortion and Stress During the Electron Beam Welding of a Low-Alloy Steel Subject to Solid State Phase Transformation," *International Journal of Mechanical Sciences,* Vol. 196, April 2021, p. 106244, doi: 10.1016/j.ijmecsci.2020.106244.
5. T.L. Bergman and A.S. Lavine, *Fundamentals of Heat and Mass Transfer,* Wiley, 2017.
6. J. Collins, M. Piemonte, M. Taylor, J. Fellowes and E. Pickering, "A Rapid, Open-Source CCT Predictor for Low-Alloy Steels, and Its Application to Compositionally Heterogeneous Material," *Metals,* Vol. 13, No. 7, June 2023, p. 1168, doi: 10.3390/met13071168.
7. M.V. Li, D.V. Niebuhr, L.L. Meekisho and D.G. Atteridge, "A Computational Model for the Prediction of Steel Hardenability," *Metall Mater Trans B,* Vol. 29, No. 3, June 1998, pp. 661–672, doi: 10.1007/s11663-998-0101-3.
8. L. Guo, H. Roelofs, M.I. Lembke and H.K.D.H. Bhadeshia, "Modelling of Recalescence Effect on Austenite Decomposition," *Materials Science and Technology,* Vol. 33, No. 10, July 2017, pp. 1258–1267, doi: 10.1080/02670836.2017.1282693.
9. A. Sugianto, M. Narazaki, M. Kogawara and A. Shirayori, "Validity of Heat Transfer Coefficient Based on Cooling Time, Cooling Rate, and Heat Flux on Jominy End Quench Test," *MS&T 2007,* 2007.
10. B. Buchmayr and J.S. Kirkaldy, "Modeling of the Temperature Field, Transformation Behavior, Hardness and Mechanical Response of Low Alloy Steels During Cooling From the Austenite Region," *J. Heat Treating,* Vol. 8, No. 2, September 1990, pp. 127–136, doi: 10.1007/BF02831633.
11. J.P. Holoman, *Heat Transfer,* 10th ed., McGraw-Hill.
12. J.S. Kirkaldy, B.A. Thomson and E.A. Baganis, "Prediction of Multicomponent Equilibrium and Transformation Diagrams for Low Alloy Steels," *Hardenability Concepts With Applications to Steel,* 1978, pp. 82–119.
13. D.P. Koistinen and R.E. Marburger, "A General Equation Prescribing the Extent of the Austenite-Martensite Transformation in Pure Iron-Carbon Alloys and Plain Carbon Steels," *Acta Metallurgica,* Vol. 7, No. 1, January 1959, pp. 59–60, doi: 10.1016/0001-6160(59)90170-1.
14. E. Scheil, "Incubation Period of Austenite Transformation," (in German) *Archiv für das Eisenhüttenwesen,* Vol. 8, No. 12, June 1935, pp. 565–567, doi: 10.1002/srin.193500186.
15. P. Maynier, B. Jungmann and J. Dollet, "Creusot-Loire System for the Prediction of the Mechanical Properties of Low Alloy Steel Products," *Hardenability Concepts With Applications to Steel,* 1978, pp. 518–544.
16. A01 Committee, "Test Methods for Determining Hardenability of Steel," doi: 10.1520/A0255-10R14.
17. K. Yamanaka and Y. Ohmori, "Effect of Boron on Transformation of Low-Carbon Low-Alloy Steels," *ISIJ Int.,* Vol. 17, No. 2, February 1977, pp. 92–101, doi: 10.2355/isijinternational1966.17.92.
18. H.K.D.H. Bhadeshia, *Bainite in Steels: Theory and Practice,* Maney Publishing, 2015.
19. X. Zhou et al., "Boron Triggers Grain Boundary Structural Transformation in Steel," *Nat Commun,* Vol. 16, No. 1, July 2025, p. 6927, doi: 10.1038/s41467-025-62264-1.
20. P. Maynier, J. Dollet and P. Bastien, "Prediction of Microstructure via Empirical Formulae Based on CCT Diagram," *Hardenability Concepts With Applications to Steel,* 1978, pp. 163–176.
21. G.T. Eldis, "A Critical Review of Data Source for Isothermal Transformation and Continuous Cooling Transformation Diagrams," *Hardenability Concepts With Applications to Steel,* 1978, pp. 126–157.
22. B. Smoljan, "Prediction of Mechanical Properties and Microstructure Distribution of Quenched and Tempered Steel Shaft," *Journal of Materials Processing Technology,* Vol. 175, No. 1–3, June 2006, pp. 393–397, doi: 10.1016/j.jmatprotec.2005.04.068.
23. E28 Committee, "Hardness Conversion Tables for Metals Relationship Among Brinell Hardness, Vickers Hardness, Rockwell Hardness, Superficial Hardness, Knoop Hardness, Scleroscope Hardness, and Leeb Hardness," doi: 10.1520/E0140-12BR19E01.
24. G. Krauss, "Martensite in Steel: Strength and Structure," *Materials Science and Engineering: A,* Vol. 273–275, Dec. 1999, pp. 40–57, doi: 10.1016/S0921-5093(99)00288-9.
25. A. Latz and A. Kern, "Modelling of Hardenability and Tempering of High-Strength Structural Steels," *HTM Journal of Heat Treatment and Materials,* Vol. 74, No. 6, December 2019, pp. 380–391, doi: 10.3139/105.110396.

This paper was presented at AISTech 2026 — The Iron & Steel Technology Conference and Exposition, Pittsburgh, Pa., USA, and published in the AISTech 2026 Conference Proceedings.